

Searching for Circular Photo Galvanic Effect in Oxyhalide Perovskite $\text{Bi}_4\text{NbO}_8\text{Cl}$

Zhizhong Chen, Rui Xu, Sijie Ma, Yuan Ma, Yang Hu, Lifu Zhang, Yuwei Guo, Zhenhan Huang, Baiwei Wang, Yi-Yang Sun,* Jie Jiang, Ryan Hawks, Ru Jia, Yu Xiang, Gwo-Ching Wang, Esther A. Wertz, Jisen Tian, Daniel Gall, Xinchun Chen, Vei Wang, Lei Gao,* Hanyu Zhu,* and Jian Shi*

The ability to reconfigure spin structure and spin-photon interactions by an external electric field is a prerequisite for seamless integration of opto-spintronics into modern electronics. In this work, the use of electric field on the tuning of circular photo galvanic effect in a quasi-2D oxyhalide perovskite $\text{Bi}_4\text{NbO}_8\text{Cl}$ is reported. The electrical transport measurements are applied to study the switching characteristics of the microsheet devices. The electric field is used to tune the nanoscale devices and an optical orientation approach is applied to understand the field-tuned spin-polarized band structures. It is found that the circular photogalvanic current can be erased and re-created by poling, indicating the electric-field-based control over spin structure. The work enriches the basic understanding of the symmetry-regulated optoelectronic response in ferroelectrics with spin-orbit coupling.

integration of different electronic functionalities and sustain the miniaturization of CMOS with spintronic technologies. It has remained the key task of the spintronics community to develop fast, energy-efficient, non-volatile, and CMOS-compatible manipulation over spin states (e.g., by magnetism) at room temperature.^[1] Currently, spin-torque-based technologies (spin transfer torque) require the assistance of current or external magnetic field during operation, thus efforts have been focused on the reduction of power dissipation and the miniaturization of magnetic coils, etc. On the other hand, voltage-based control over spin, electric polarization, etc. show much lower power

1. Introduction

The spin degree of freedom of electron, which intrinsically mimics the 0 and 1 logic states, is believed to enhance the

consumption than current-assisted methods.^[2]

At present, the room-temperature voltage-based control of spin, especially magnetism (i.e., magnetoelectric coupling), mainly relies on the niche heterostructures incorporating

Z. Chen, Y. Hu, L. Zhang, Y. Guo, Z. Huang, B. Wang, J. Jiang, R. Hawks, R. Jia, D. Gall, J. Shi
Department of Materials Science and Engineering
Rensselaer Polytechnic Institute
Troy, NY 12180, USA
E-mail: shij4@rpi.edu

R. Xu, S. Ma, H. Zhu
Department of Materials Science and NanoEngineering
Rice University
Houston, TX 77005, USA
E-mail: hanyu.zhu@rice.edu

Y. Ma, L. Gao
Beijing Advanced Innovation Center for Materials Genome Engineering
Institute for Advanced Materials and Technology
University of Science and Technology Beijing
Beijing 100083, China
E-mail: gaolei@ustb.edu.cn

Y.-Y. Sun
State Key Lab of High Performance Ceramics
and Superfine Microstructure
Shanghai Institute of Ceramics
Chinese Academy of Sciences
Shanghai 201899, China
E-mail: yysun@mail.sic.ac.cn

 The ORCID identification number(s) for the author(s) of this article can be found under <https://doi.org/10.1002/adfm.202206343>.

Y. Xiang, G.-C. Wang, E. A. Wertz
Department of Physics
Applied Physics
and Astronomy
Rensselaer Polytechnic Institute
Troy, NY 12180, USA

J. Tian, X. Chen
State Key Laboratory of Tribology
Tsinghua University
Beijing 100084, China

V. Wang
Department of Applied Physics
Xi'an University of Technology
Xi'an 710054, China

J. Shi
Center for Materials
Devices, and Integrated Systems
Rensselaer Polytechnic Institute
Troy, NY 12180, USA

DOI: 10.1002/adfm.202206343

magnetic materials that could break inversion symmetry and time reversal symmetry simultaneously.^[3] The scarcity of room-temperature single-phase magnetoelectric multiferroics mainly stems from its stringent requirements on electron configuration.^[4] The use of magnetic heterostructures, though enhances the magnetoelectric conversion efficiency by orders of magnitudes compared to single-phase multiferroics,^[5] inevitably adds complexity into device fabrication and compromises the compatibility with CMOS. More discussions on magnetoelectric coupling are given in Discussion S1 and Figure S1 (Supporting Information).

Rather than resorting to magnetic systems, the electric-field control over spin can be achieved in non-magnetic strong-spin-orbit-coupling (SOC) systems. Rashba SOC, a phenomenon in semiconductors lacking inversion symmetry, is manifested as an effective magnetic field B_{eff} imposed onto charges. The B_{eff} , sometimes as large as a few T in III–V quantum wells,^[6] is capable of spin manipulation and has led to various spintronic phenomena (e.g., persistent spin helix^[7]). The Rashba SOC field B_{eff} scales with \vec{p} the electron momentum and \vec{E} the electric field:^[7,8]

$$\vec{B}_{\text{eff}} \sim \vec{p} \times \vec{E} \quad (1)$$

In a crystal, the electric field \vec{E} may stem from external symmetry breaking with hetero-interface (e.g., Rashba interface like SrTiO₃/LaAlO₃ 2D electron gas^[9]) or a gating voltage (e.g., in Datta–Das spin FET^[10]), or the intrinsic electric field in inversion asymmetric crystals (e.g., in bulk ferroelectrics^[11]). Importantly, for strong-SOC materials or heterostructures with electric-field-tunable symmetry breaking, their B_{eff} can be flipped instantly by flipping electric dipoles, which are non-volatile, voltage-controlled, and energy-efficient. These proposals have incubated the field of spin-orbitronics,^[12] which exploits the charge/spin currents in strong-SOC nonmagnetic systems including Rashba interfaces, topological insulators, and bulk ferroelectrics.

While a single-phase Rashba ferroelectric material seems the most straightforward solution, the spintronics community is still searching for a qualified candidate that meets all the requirements, including robust room-temperature ferroelectricity down to nm dimensions, low defect concentration, proper bandgap, and strong SOC. Although spin-split band structure (i.e., spin texture) and its correlation with ferroelectric polarizations have both been observed in GeTe at room temperature,^[13] the leaky nature of GeTe has so far complicated the ferroelectric switching.^[13c] Oxide ferroelectrics usually carry strong electric dipoles robust at room temperature;^[14] some of which were predicted to show exquisite spin structures such as switchable persistent spin helix. Nevertheless, the insulating nature of these strong-SOC oxide ferroelectrics (e.g., BiAlO₃,^[15] CsBiNb₂O₇^[16] and HfO₂^[17]) have further complicated their spintronic applications as the conduction media.

Here we report an electric-field-tunable spin-photon interaction in a quasi-2D oxyhalide perovskite Bi₄NbO₈Cl. Bi₄NbO₈Cl has a bandgap ≈ 2.6 eV within visible light regime^[18] and exhibits a Dresselhaus-type spin texture near conduction band minimum. Importantly, Kusainova et al have observed in Bi₄NbO₈Cl a reversible polar-to-centrosymmetric ferroelectric-type transition (from P2₁cn to Pmcn) at ≈ 765 K by impedance

spectroscopy and second harmonic generation (SHG).^[19] These conditions have enabled the reconfigurable spin-photon interactions at metal–Bi₄NbO₈Cl interface such that the circular photogalvanic effect (CPGE) in Bi₄NbO₈Cl single crystalline microsheet devices can be tuned by electric field.

1.1. Structural Symmetry and Spin-Polarized Electronic Structure

A favorable crystal symmetry class to generate a neat Dresselhaus-type spin texture is C_{2v} point group (symmetry elements include two mirror planes $x\text{-}y$ and $x\text{-}z$, and a C₂ axis along x). It has been derived that $B_{\text{eff}}(k)$ is canceled out everywhere except along z , and in turn the single-paraboloid electron $E\text{-}k$ dispersion is modified, neglecting cubic term, to a double-paraboloid dispersion following

$$H = \frac{\hbar^2}{2m^*} (k_x^2 + k_y^2) + \alpha_D k_y \sigma_z \quad (2)$$

where α_D the Dresselhaus coefficient and σ_z Pauli matrix.^[7,20]

The reciprocal unit cell of the proposed material Bi₄NbO₈Cl (under C_{2v} point group, P2₁cn space group) is shown in Figure 1a,b (the real space cell is shown in Figure 1c): the 2₁ axis shown by the orange/blue arrows as well as the electric dipoles are along $\Gamma \rightarrow X$. If the polarity of the electric dipoles at crystal surface is switched, the polarity of the 2₁ axis switches as well. Based on Equation (1), the direction of B_{eff} is determined by the direction of electric field, indicating that the switching of electric dipoles will eventually switch B_{eff} and modulate the spin structure.

Figure 2 shows the density of states of individual orbitals in Bi₄NbO₈Cl. The band composition indicates that CBM and VBM are mainly composed of Bi 6p orbital and O 2p orbital, respectively. The higher percentage of heavy-element-derived CBM than VBM suggests a stronger SOC effect in CBM.^[21] The Cl 3p orbital mainly contributes to VB which is largely responsible for the narrowing of bandgap compared to the oxide counterparts.

We then synthesized single crystals to verify the electric dipole-related spin structure. A-hundred-micrometer-scale individual single crystals Bi₄NbO₈Cl were grown by high-temperature solid-state reaction (see Experimental Section for details). Individual rectangular disks with lateral size 5 to 20 μm and thickness ≈ 2 μm were synthesized by flux method. The energy-dispersive X-ray (EDX) analysis on a typical rectangular disk shows the atomic ratio of Bi/Nb/O/Cl is 4.37/1.26/8.61/1, respectively, consistent with the expected stoichiometry. X-ray diffraction (XRD) of bulk single crystal and microcrystals grown by a salt flux are shown in Figure 3a. The bulk crystal shows only (004), (008), (0010), (0012), and (0014) peaks, indicating its single-crystalline nature. The XRD pattern from flux-grown micro crystals turns out highly consistent with simulation, with the strongest peak being (116) and only one tiny impurity peak at $2\theta \approx 29^\circ$.^[18e] Bulk Bi₄NbO₈Cl single crystals were mechanically exfoliated (the product hereafter referred to as “microsheets”) and transferred onto different substrates. Based on atomic force microscopy (AFM, Figure S2a, Supporting Information), most microsheets are 100–300 nm thick, with lateral dimensions of 10 to 40 μm . Probably due to high exfoliation energy, Bi₄NbO₈Cl microsheets thinner than 10 nm are rare, different

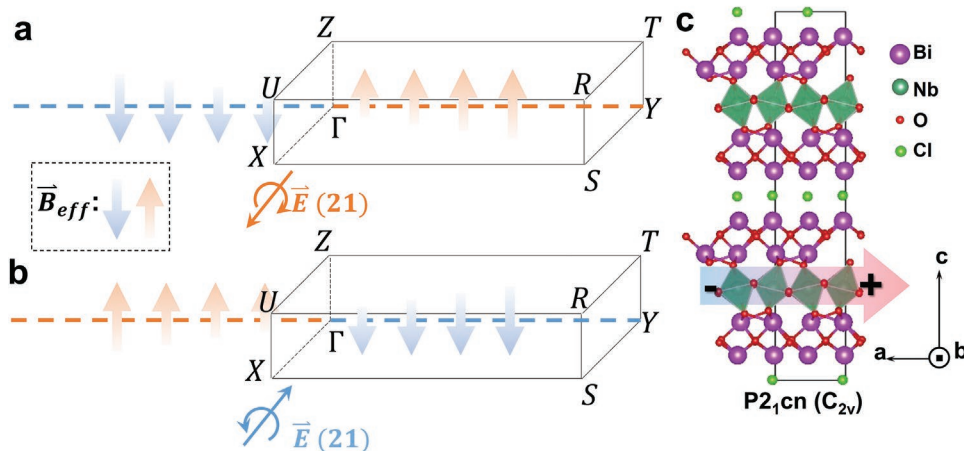


Figure 1. Reconfigurable effective magnetic field \vec{B}_{eff} in a strong-spin-orbital-coupling material with switchable surface electric dipoles. a) Electrons moving in strong-SOC system undergo an effective magnetic field \vec{B}_{eff} which scales with $\vec{p} \times \vec{E}$ where \vec{p} the electron momentum and \vec{E} the internal electric field the electrons feel. For electrons moving within the x - y plane inside a crystal derived from C_{2v} point group, the \vec{E} goes along $\Gamma \rightarrow X$ and a unidirectional \vec{B}_{eff} is expected along $\Gamma \rightarrow Z$, eventually generating a Dresselhaus-type spin texture. b) When \vec{E} switches direction, the \vec{B}_{eff} associated with it will reverse accordingly, enabling the electric-field-based control over spin structure. c) the crystal structure of the proposed material Bi_4NbO_8Cl whose room temperature $P2_1cn$ phase is derived from C_{2v} point group. The colored arrow shows the electric dipoles of Bi_4NbO_8Cl along its a -axis

from other layered oxides like $Bi_2Sr_2CaCu_2O_{8+\delta}$.^[22] The layered structure of exfoliated Bi_4NbO_8Cl single crystalline microsheets was further confirmed by HRTEM. As shown in Figure 3b and its insets, the high-resolution image clearly shows the parallel lattice fringes. Based on selected area electron diffraction (SAED) shown in Figure S2b (Supporting Information), the lattice constant c was calculated to be 2.935 nm, consistent with reference value.^[18e] All the following transport measurements were conducted with microsheets exfoliated from single crystals grown by solid-state reaction.

Due to the technical challenges in the P - E loop measurement of low-dimensional ferroelectrics with in-plane electric dipoles,^[23] we monitored the response of its pyroelectric coefficient to DC poling voltage in a parallel-plate-capacitor type device made with a sintered polycrystalline ceramic disk. Before the test, the ceramic disk device was first poled. After removing poling voltage, we measured the pyroelectric coefficient by monitoring the current released by the device upon heating/cooling. As Figure 3c shows, after a 5 min poling under 3000 V, the device showed a negative pyroelectric current during the heating process, while it showed a positive pyroelectric current after poling with -3000 V for 5 min. The device was then poled under a series of different voltages. Eventually, we received the effective pyroelectric coefficient versus poling electric field hysteresis loop given in Figure 3d. Since the averaged pyroelectric coefficient of the device scales with the ferroelectric dipoles,^[24] the switchability and hysteresis of pyroelectric coefficient serve as a side evidence of switchable electric dipoles in Bi_4NbO_8Cl .

To further understand the domain structure in Bi_4NbO_8Cl , we performed SHG mapping with details given in Experimental Section and Figure 3e. Basically, the exfoliated flake with (001) plane exposed, optical image given in Figure 3f, is scanned by a focused, linearly polarized pulsed laser beam at normal incidence with center wavelength of 798 nm, and the reflected SHG signal at 399 nm is detected after a fixed polarizer. The polarization of the incident beam is set to an angle of φ with respect to the detection polarization. Figure 3g,h show the SHG mapping on the exfoliated Bi_4NbO_8Cl microsHEET with $\varphi = 0^\circ$ and 90° , respectively. Figure S3a-c (Supporting Information) shows another set of SHG mappings on this crystal performed at 519 K, exhibiting similar domain patterns. Domains with high (low) SHG intensity turned to low (bright) intensity after increasing φ from 0° to 90° , and the intensity could be recovered after resetting φ to 180° . Based on the symmetry analysis given in Discussion S2 (Supporting Information), the polarization of

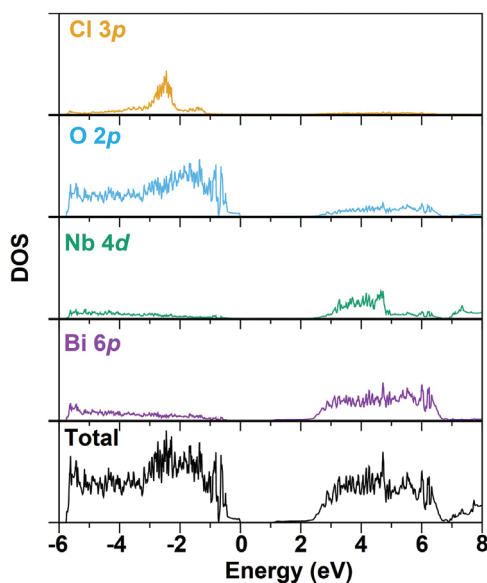


Figure 2. Calculated electronic density of states of Bi_4NbO_8Cl , showing strong Bi contribution that causes large spin-orbit coupling in the conduction band.

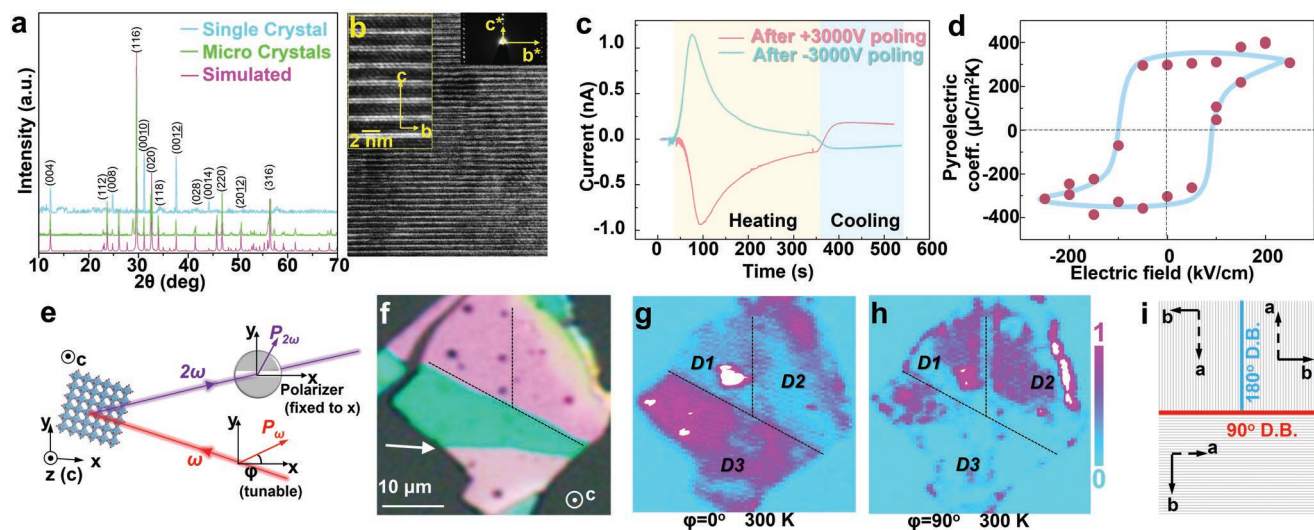


Figure 3. Structural characterizations of $\text{Bi}_4\text{NbO}_8\text{Cl}$. a) XRD of bulk single crystal and microcrystals. b) Main figure and upper left inset: HRTEM of $\text{Bi}_4\text{NbO}_8\text{Cl}$ microsheet. c) Pyroelectric current of poled $\text{Bi}_4\text{NbO}_8\text{Cl}$ ceramic disk upon cooling or heating. d) Pyroelectric coefficient by integrating the pyroelectric current upon poling at different voltages. The pyroelectric coefficient changed and showed hysteretic behavior with respect to poling voltages. e) The setup of SHG measurement. f) An optical image of an exfoliated microsheet subjected to SHG mapping. The white arrow marks a boundary line which is caused by thickness contrast rather than different crystallographic orientations. g, h) SHG mapping at room temperature with polarization angle $\varphi=0^\circ$ or $\varphi=90^\circ$. The three domains revealed from SHG mapping are marked D1, D2 and D3. i) illustration of 90° and 180° domain boundaries.

SHG signal is supposed to be along [100] and [010] of $\text{Bi}_4\text{NbO}_8\text{Cl}$. Therefore, the change of SHG intensity in Figure 3g,h and Figure S3a–c (Supporting Information) can be explained by the formation of 90° domain boundaries sketched in Figure 3i, which are common among ferroelectrics whose in-plane lattice constants are close. In another exfoliated microsheet, shown in Figure S3d (Supporting Information), the SHG mapping showed alternating parallel patterns with typical width $\approx 2 \mu\text{m}$, which can be attributed to the destructive interference at 180° domain boundaries.^[25] Optical properties are further exploited by photoluminescence shown in Figures S4 and S5 (Supporting Information). The optical properties of layered oxide perovskites were studied extensively in recent years.^[26] $\text{Bi}_4\text{NbO}_8\text{Cl}$ shows a wide luminescence peak centered at 600 nm, and room-temperature carrier recombination lifetime $\approx 2 \text{ ns}$. The large peak widths are common among transition metal oxide perovskites.^[27] Temperature-dependent time-resolved photoluminescence is given in Figure S6 (Supporting Information).

1.2. In-Plane Electric Dipole Switching

Single crystalline microsheets were assembled into microdevices with either graphite flakes or conductive oxides as chemically inert electrodes so that metal filament formation or grain boundary effects can be avoided (see Experimental Section and Figure S7, Supporting Information for details). Device 1 was fabricated with two graphite electrodes and a channel length $\approx 30 \mu\text{m}$. As sketched in Figure S7 (Supporting Information), the microsheet was exfoliated along (001) plane such that the electric dipoles (along a axis) are distributed within the microsheet plane rather than along the plane normal. This in-plane configuration is different from typical vdW ferroelectric materials. Under $\pm 5 \text{ V}$ sweep (sweeping rate 0.2 V s^{-1}), Device

1 yielded a dark current up to 4 nA, and the whole I – V curve showed a non-linear profile. Dark current density is roughly $0.25 \text{ nA } \mu\text{m}^{-1}$ under +5 V bias. After illuminating the crystal with laser beam (continuous wave, center wavelength 405 nm, output power $\approx 4 \text{ mW}$, spot size $\approx 3 \text{ mm} \times 3 \text{ mm}$), the current increased by ≈ 100 times. More photo response studies are shown in Figure S8 (Supporting Information). The top surfaces of newly exfoliated crystals were scanned with high-resolution atomic force microscopy (HRAFM) shown in Figure 4b,c. Based on the lattice information, Figure 4b shows the topmost layer is Bi atom arrays while Figure 4c shows oxygen atom arrays possibly covering the topmost surface. The ultrathin crystal with incomplete unit cell termination thus could behave differently from its bulk phase.

We then probe the in-plane dipole switching at metal– $\text{Bi}_4\text{NbO}_8\text{Cl}$ interfaces by switchable diode effect illustrated in Figure 4d.^[28] It is anticipated that the virgin state $\text{Bi}_4\text{NbO}_8\text{Cl}$ microsheet has randomly oriented dipoles, leading to symmetric Schottky barriers Φ_0 at both interfaces. After poling, the energy bands near surfaces are shifted upward/downward by Φ_p due to the negative/positive charges from oriented dipoles, thus asymmetric Schottky barriers ($\Phi_0 \pm \Phi_p$) are formed at two interfaces.

A short-channel device is more favorable for the revelation of interfacial properties since the large resistance of a long channel, such as that of Device 1, may easily mask any plausible resistance modulation from the dipoles at electrode– $\text{Bi}_4\text{NbO}_8\text{Cl}$ interface. Therefore, we fabricated Device 2 with only $\approx 4 \mu\text{m}$ channel whose structure is sketched in Figure 4e (optical image given in Figure S7, Supporting Information). It should be noted that the dipoles along a axis distribute within the microsheet plane. To avoid the breakdown of air within the channel the two graphite electrodes were intentionally placed on different surfaces of the microsheet. Since the thickness of the microsheet ($\approx 100 \text{ nm}$) is still much smaller than channel length, the

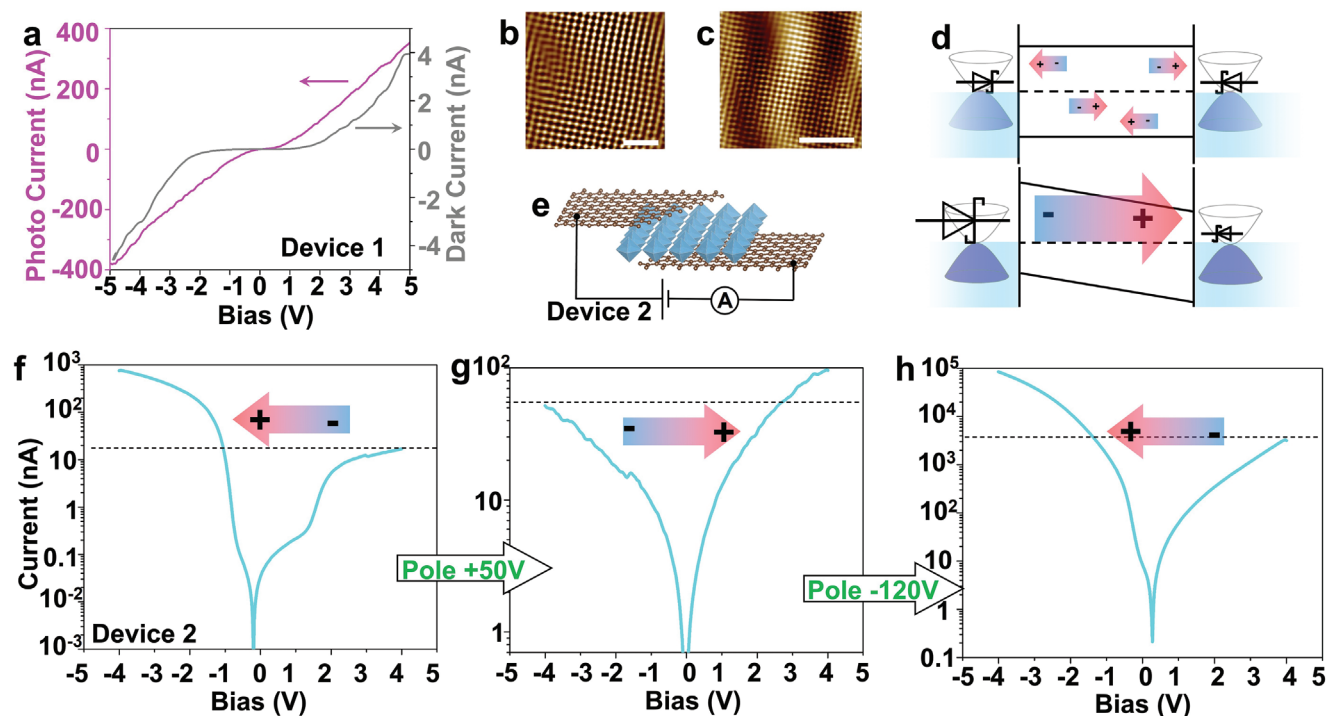


Figure 4. The switching of surface electric dipoles on $\text{Bi}_4\text{NbO}_8\text{Cl}$ microsheets probed by switchable diode effect. a) Dark and photocurrent of a $\approx 30\text{-}\mu\text{m}$ -channel planar device (Device 1) under -5 V to $+5\text{ V}$ bias, showing the significant photo response. HRAFM images reveal that the crystal surfaces could be b) Bi-terminated or c) O-terminated. Scale bar: 2 nm for both (b) and (c). d) Switchable Schottky diode effect in a ferroelectric insulator with in-plane dipoles and symmetric electrodes. Upper sketch, virgin state with random ferroelectric dipole orientation. The two Schottky barriers are of same height. Lower sketch, after poling the dipoles are aligned with preferred orientation, leading to asymmetric charge distribution at the crystal surfaces, and in turn leads to asymmetric Schottky barrier heights at the two interfaces. The barrier height is represented by the size of Schottky diode symbols. e) Sketch of device 2 with $2\text{-}\mu\text{m}$ channel and two graphite electrodes on different surfaces of $\text{Bi}_4\text{NbO}_8\text{Cl}$. The $\text{Bi}_4\text{NbO}_8\text{Cl}$ crystal is represented by a layer of octahedral for simplicity. The switching of in-plane dipoles probed by switched rectification in the $2\text{-}\mu\text{m}$ -channel device (Device 2). f) Diode behavior was induced by unintentionally aligned dipoles pointing to negative direction. g) The diode polarity and dipole orientation in e were both switched by poling with $+50\text{ V}$. h) The diode behavior in f was switched again by poling with -120 V . The polarity went back to that in (f).

electric field within the channel of Device 2 is predominantly in-plane.

Figure 4f shows the dark current of Device 2 without intentional poling which showed significant rectification. After poling under $+50\text{ V}$ for 15 min , the reverse current decreased by ≈ 20 times (from -900 nA to -50 nA), while the forward current increased by ≈ 5 times, from 20 nA to 100 nA , Figure 4g. After a second poling under -120 V for 15 min , the rectification was reversed again, and both forward and reverse currents are ≈ 100 times in magnitude of those in Figure 4f. It should be noted that all the rectifications from the three stages were stable under repeated scans and are hysteresis-free, indicating that the observed phenomenon may not be due to ion migration or other defect-induced processes^[29] (repeated scans of Device 2 are given in Figure S9a, Supporting Information).

It is possible, at the initial stage, the dipoles induced upward/downward band bending on either interfaces and caused the rectification (Figure 4f). The $+50\text{ V}$ poling was then able to reverse some of dipoles such that the Schottky barriers on both interfaces were nearly eliminated. The residual barrier, however, still induced minor rectification shown in Figure 4g. After the -120 V poling, the interfaces status in Figure 4f was almost recovered except for some differences in barrier height which led to the much higher current amplitudes in both

directions. The complicated interface structure and the unknown ferroelectric switching dynamics such as commonly observed wake-up effect or imprint effect in oxides^[30] for this relatively new material probably hindered the dipole switching and in turned caused the asymmetric barrier modulation in all stages. For example, the existence of imprint effect^[31] in ferroelectric materials leads to asymmetric switching barrier (one polarization state is more energetically favored than the opposite) which would bring asymmetric transport characteristics. We also fabricated devices with $\approx 40\text{-nm}$ -thick and 8-nm -thick microsheets (corresponding to ≈ 13 and 3 unit cells, respectively, given in Figures S10 and S11, Supporting Information). Although both microsheets became more insulating, switchable rectification was observed in the 13 -unit-cell thick device and unswitchable rectification was observed in a ≈ 3 -unit-cell device. The salient change of transport properties at reduced channel thickness might stem from the unfavorable distribution of screening electric field or the change of intrinsic properties of $\text{Bi}_4\text{NbO}_8\text{Cl}$ at ultra-thin limit. The variation in surface termination and incomplete topmost unit cell shown in HRAFM in Figure 4b,c might influence the overall property of microsheat, e.g. by inducing different degrees of imprint effect.

Although the switchable Schottky diode effect suggests the reconfigurability of interface electric dipoles of $\text{Bi}_4\text{NbO}_8\text{Cl}$

microsheets, whether $\text{Bi}_4\text{NbO}_8\text{Cl}$ microsheet rigorously carries ferroelectricity remains elusive. In addition to the parasitic capacitance effect in non-parallel-plate-capacitor devices, the displacive current generated by ferroelectric dipole switching of ultrathin in-plane ferroelectrics can be easily overwhelmed by the switchable diode effect, making any observed P - E loop a false alarm for ferroelectricity.^[28f] Therefore, after confirming the tunability of the electric dipoles at metal- $\text{Bi}_4\text{NbO}_8\text{Cl}$ interfaces, we next focus on the correlation between dipole switching and spin texture which was probed by circular photogalvanic effect (CPGE).

1.3. CPGE

A powerful tool to monitor the spin-dependent optical transitions is CPGE. In strong-SOC systems the optical transition is governed by the conservation of total angular momentum

$J = S + L$ where S and L are spin and angular momentum. As sketched in Figure 5a, left circularly polarized light that carries spin angular momentum $S = +\hbar$ is able to excite electrons into specific local minima of CB, while the mirrored transition can be achieved by right circularly polarized light that carries spin angular momentum $S = -\hbar$. Such momentum-photon locking leads to spin-dependent optical transitions in reciprocal space which reflects the spin texture of $\text{Bi}_4\text{NbO}_8\text{Cl}$. Microscopically CPGE is enabled by the angular momentum of photons transferred into a translational motion of charge carriers.^[32] CPGE current is supposed to scale as $\sin 2\varnothing$ where \varnothing stands for the polarization angle of incident light. Namely, $\varnothing = 0^\circ$ or 90° corresponds to linearly polarized light, both carrying only linear momentum; while $\varnothing = 45^\circ$ or 135° corresponds to right/left circularly polarized light, carrying opposite angular momentum.^[32a] Thus the CPGE currents generated by left/right circularly polarized light are of same amplitude but along opposite directions.

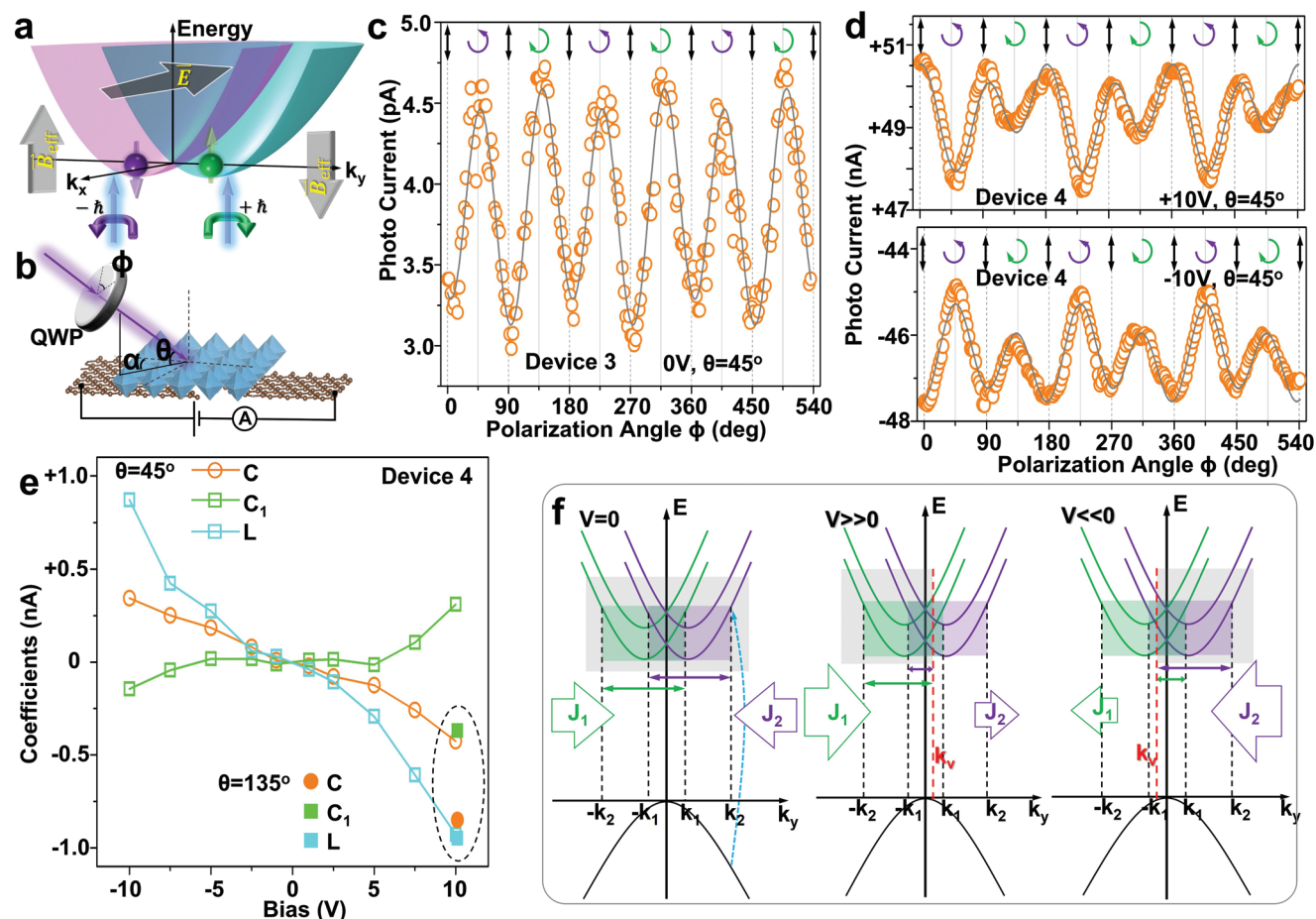


Figure 5. Circular photogalvanic effect (CPGE) in $\text{Bi}_4\text{NbO}_8\text{Cl}$. a) Principle of spin-selective optical transitions in $\text{Bi}_4\text{NbO}_8\text{Cl}$. B_{eff} lifts spin degeneracy and induces double-paraboloid band structure. When excited with circularly polarized light carrying angular momentum of $+\hbar$ or $-\hbar$ (shown by vertical glowing arrows), electrons with $k_y > 0$ or $k_y < 0$ can be selectively excited into CBM. b) A sketch of photogalvanic measurement. The quarter-wave plate (QWP) is rotated continuously to change the helicity of incident laser beam. The $\text{Bi}_4\text{NbO}_8\text{Cl}$ crystal is represented by a layer of octahedral for simplicity. c) Short-circuit CPGE signal in Device 3. Measured data points are shown as open orange circles while the fitting curve is drawn as solid gray curve. d) CPGE signal detected in Device 4 under ± 10 V bias. e) In device 4, when bias was changed continually between -10 V to $+10$ V, the fitting coefficients C , C_1 , and L all scale as odd function of bias. The results with incidence angle $\theta = 45^\circ$ or 135° are drawn as open and closed symbols, respectively. f) Proposed influence of bias on CPGE, where J_1 and J_2 indicate the current generated from right/left circularly polarized light respectively, due to the asymmetric distribution of photo-generated carriers in momentum space.

A phenomenological description of polarization-dependent photo current is given below,

$$I(\varnothing) = C \sin 2\varnothing + C_1 \cos 2\varnothing + L \sin(4\varnothing + \delta) + D \quad (3)$$

where C stands for the CPGE term. The C_1 could come from the setup of the optics.^[34] The other sinusoidal term $L \sin(4\varnothing + \delta)$ represents linear photogalvanic effect (LPGE) and linear photon drag effect (LPDE). Both LPGE and LPDE are related to the linear angular momentum of photons and are not related to spin.^[33] The phase factor δ characterizes the accumulative contributions of LPGE and LPDE terms. The last term D is a polarization-independent current. More discussions about CPGE are provided in Discussion S4 (Supporting Information).

It should be emphasized that among all these terms, only $C \sin 2\varnothing$ reflects the intrinsic helicity dependence and will be our focus of following discussions. When the spin structure of the material switches, the sign of C is supposed to switch as well. In other words, we will monitor the amplitude and sign of C via photo current measurements so as to monitor the spin structure of $\text{Bi}_4\text{NbO}_8\text{Cl}$.

As illustrated in Figure 5b, in CPGE measurements a micro device was illuminated by laser beam (continuous wave, center wavelength 405 nm, output power ≈ 4 mW, spot size ≈ 3 mm \times 3 mm) with a quarter wave plate (QWP) inserted in the middle, and the short-circuit or biased photo current as a function of polarization angle \varnothing (the angle between the fast axis of QWP and the polarization plane of laser beam) was recorded. Incident angle θ was chosen among 45, 90, or 135° while azimuthal angle α was fixed. The short-circuit CPGE was successfully detected in Device 3 with two graphite electrodes on top and bottom of the crystal, Figure 5c. As the fitting curve shows, a weak CPGE current ≈ 0.2 pA is evident by the periodically modulated photo current under right/left circularly polarized lights. The weak CPGE might be caused by the difficulties in charge carrier separation or extraction, as often observed in transition metal dichalcogenides.^[33a] More details about CPGE of Device 3 are given in Figure S12 (Supporting Information). We therefore checked the biased photo current in Device 4 (with both graphite electrodes beneath the crystal). As shown in Figure 5d, with ± 10 V bias the photo current excited by right/left circularly polarized lights differed by ≈ 1 nA, much larger than the short-circuit case in Device 3. Fitting results of Device 4 under different bias are summarized in Figure 5e. When incidence angle θ was fixed at 45°, C , C_1 and L all behaved as odd function of bias. It should be noted that though C term was reversed upon reversing bias, right circularly polarized light was always able to generate more carriers than left circularly polarized light. When incident angle θ was changed to 135°, C_1 term reversed while the sign of C and L terms remained. Further analysis in Figure S13 (Supporting Information) shows that the trend in L term is dominated by $(L \sin \delta)$ while no explicit response to bias could be captured from $L \cos \delta$. At normal incidence ($\theta = 90^\circ$), the results are shown in Figure S13, Supporting Information, which could be complicated by the presence of interface or surface^[32,35,36] The rather distinct responses of C and L terms to measurement geometry indicates that the modulation of photo current indeed reflects the intrinsic helicity selection in $\text{Bi}_4\text{NbO}_8\text{Cl}$ derather than experiment

artifacts (e.g., change of incident light intensity). More discussions about CPGE of Device 4 are given in Discussion S4 (Supporting Information).

As illustrated in Figure 5f, the role of bias on CPGE is tentatively inferred from their mechanisms under short-circuit condition.^[32,37] We first hypothesize that bias will not change the intrinsic band structure of the material (e.g., band curvature), and all the charge carriers generated can be extracted into external circuit. A typical band structure with spin splitting in CB is sketched in Figure 5f. The spin up/down branches of CB are drawn green/purple, respectively, while the spin splitting in valance band is omitted for simplicity. For short-circuit condition ($V = 0$, Figure 5f left), after excitation with left/right circularly polarized light the regions marked by solid horizontal purple/green arrows (covering $-k_2$ to k_1 or $-k_1$ to k_2) can be occupied by photo-excited electrons. Due to the asymmetric distribution of electron momentum in each case, a net short-circuit current J_1 or J_2 is generated by left/right circularly polarized lights, respectively. It should be note that for each case the electrons excited into CB will leave behind the same number of holes in VB. Since the electrons and holes share the same momentum while carry opposite charges, the currents induced by these pairs tend to cancel out each other. However, due to the different transport characteristics, like doping concentration, mobility and lifetime of electrons and holes, a complete cancellation is impossible and a net CPGE current can still be generated from either electrons or holes. Since the spin splitting is mainly within CB, we hypothesize that the net current is dominated by electrons in CB which qualitatively should not change the conclusions. Based on symmetry, J_1 or J_2 are along opposite directions but of equal magnitude. An external bias is supposed to shift the distribution of available density of states in k space, marked by the gray rectangle in conduction band.^[32b,38] When a large positive bias is applied ($V \gg 0$, Figure 5f middle) the boundary of available states could be shifted to k_v such that the photo-excited electrons are redistributed in k space. As a result, for both J_1 and J_2 the electrons carrying positive k_v are reduced, thus J_1 is increased while J_2 is reversed. The scenario for high negative bias ($V \ll 0$, Figure 5f right) can be understood in a similar way where J_2 is increased and J_1 is reversed. It should be noted that for small positive bias such that $k_v > k_2$ (or small negative bias such that $k_v < -k_2$), the shift in density of states is not large enough to redistribute photo-excited electrons and J_1 or J_2 will not change. Since the CPGE coefficient C is defined as half of the difference between the photo current under pure right and left circularly polarized lights, i.e., $C = (J_1 - J_2)/2$, we expect that C will decrease in a transition region but will not change sign even for high enough bias, as sketched in Figure S14, Supporting Information. Based on this simplified argument CPGE current should neither reverse sign nor scale linearly with bias. However, we observed rather different phenomena, indicating that the role of bias is more complicated and the aforementioned two assumptions do not hold. For example, the symmetry of monolayer MoSe_2 was observed to be switched from a single mirror plane to C_{3v} when bias exceeded ≈ 0.5 V.^[34a] Also, in monolayer MoS_2 or gated multilayer WSe_2 CPGE current scaled linearly with bias, the change of photo currents under bias being attributed to the improved carrier separation/extraction.^[33] In our case, we suppose that bias does

facilitate carrier extraction, and in addition to the switching of electric dipoles, the bias might also induce other types of symmetry breaking that scales monotonically with the bias applied (similar to the control of Rashba field by gate voltage in some III–V heterostructures^[39]).

1.4. Electric-Field Tuning of CPGE

Although the exact role of bias on CPGE remains unknown, CPGE under bias partially evidences the spin texture in $\text{Bi}_4\text{NbO}_8\text{Cl}$. Next we explore the electric-field control of spin texture from the change of CPGE. **Figure 6a–e** shows the dark current scans of Device 5 (one graphite electrode and one LSMO electrode, both beneath the crystal, channel length $\approx 5 \mu\text{m}$). At initial state a near-linear and symmetric dark current up to $\pm 10 \text{ pA}$ was observed. As shown in inset of Figure 6a, no explicit CPGE signal could be resolved at this stage under ± 10 or 0 V (details in Figure S15, Supporting Information). During repeated dark I – V scans the current generated under reverse bias suddenly increased by ≈ 100 -fold, approximately from -10 nA to -1 nA , while the forward-bias part stayed roughly the same. The new state after this sudden change is plotted as Figure 6b. The salient change in rectification during dark current scans may be due to unintentional domain switching triggered probably by local high electric fields or repeated perturbation during dark I – V scans. As shown in Figure 6f, CPGE current was created along with the creation of rectification. Then after being poled under $+40 \text{ V}$ for 15 min, Device 5 became highly insulating in both directions, yielding a symmetric and linear dark current up to $\pm 5 \text{ pA}$, Figure 6c. Although the $+40 \text{ V}$ poling erased the rectification in Figure 6c, the CPGE current was not altered and shown in Figure 6g. Although the dark current under reverse bias in Figure 6c is ≈ 200 times smaller than

that in Figure 6b, the photo currents under -10 V in these two stages are both within 10 – 20 nA . This discrepancy indicates that the rectifications induced by Schottky barriers at interfaces are overwhelmed by the abundance of carriers at illuminated condition. Indeed in Figure 4a the photo current shows a much more linear dependence to bias than that of dark current. Next, Device 5 was poled under -40 V for 15 min and dark current became slightly higher and nonlinear in both directions, up to $\pm 20 \text{ pA}$, while CPGE current was erased again as in Figure 6d inset. After more scans in dark, as shown in Figure 6e,h, the reverse current suddenly increased and both I – V and CPGE recovered to the previous stage shown in Figure 6b,f. It should be noted that the CPGE current in Figure 6h was measured under $+10 \text{ V}$ but based on the bias dependence analyzed before the CPGE currents in Figure 6b,f,e,h are of similar nature. Throughout the whole measurement Device 5 remained equally high photo response thus no device degradation occurred.

The erasing of CPGE is likely due to a random distribution of domains rather than the absence of Rashba–Dresselhaus effect. We sketch the possible domain orientation of the five stages shown in Figure 6a–e in their insets. In each inset, the smaller arrows near the interface and the larger arrows closer to the channel center represent those pertinent to Schottky barrier modulation and CPGE modulation, respectively. The I – V rectification can be understood as in Device 2 while the discrepancies in the magnitudes of dark currents between Device 5 and 2 may stem from the device geometries. As for CPGE, the domain involved oriented randomly in the initial stage Figure 6a, and then aligned by the first sweep, further aligned by the $+40 \text{ V}$ poling, then randomized by the -40 V poling, finally the orientation got recovered through the second sweep. Consequently the CPGE was able to be created, erased and created again by sweeping or poling.

Despite the demonstration of electric-field-based control of CPGE in $\text{Bi}_4\text{NbO}_8\text{Cl}$, the control over CPGE is still impeded

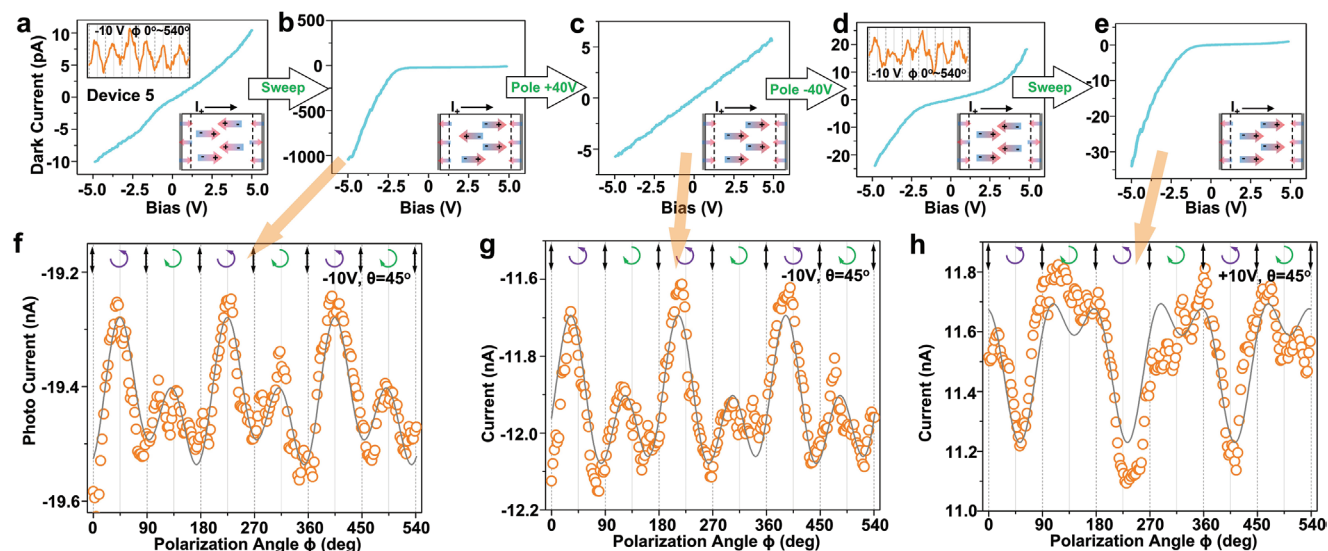


Figure 6. Tuning of CPGE in $\text{Bi}_4\text{NbO}_8\text{Cl}$ Device 5 through DC poling. a–e) Dark current in Device 5 is manipulated by sweeping or poling. The CPGE signal of (a), (d) are shown as insets therein, while CPGE signals of stages (b), (c), and (e) are shown separately as (f), (g), and (h), respectively. The possible domain orientations are also shown as insets of (a–e), where the gray shades indicate electrodes, and the black horizontal arrow shows the reference direction of current. Net CPGE signal was negligible in (a), created in (b,c) after positive polings, erased in (d) by negative poling, and eventually recovered in (e) by the second sweeping.

by a few factors. First, the microscopic mechanisms of the switching dynamics and asymmetric switching of $\text{Bi}_4\text{NbO}_8\text{Cl}$ are largely unknown. Second, based on symmetry, the CPGE current is generated perpendicular to the electric polarization direction while the electrodes in our devices possibly collect currents from many in-plane directions (detailed in Figure S16, Supporting Information). The change in CPGE signal would be largely averaged out by current along other directions. Third, the plausible in-plane ferroelectricity in $\text{Bi}_4\text{NbO}_8\text{Cl}$ further complicates the poling and device design. Similar challenges have been found to appear in many other 2D ferroelectrics.^[23]

2. Conclusion

In this work we propose an oxyhalide semiconductor $\text{Bi}_4\text{NbO}_8\text{Cl}$ with strong SOC, unique symmetry and reasonable chemical stability as a potential candidate to electric-field-based nonvolatile control over spin texture. The nanoscale devices based on $\text{Bi}_4\text{NbO}_8\text{Cl}$ exhibit asymmetric switching characteristics. We have demonstrated the possible reconfigurability of the CPGE of $\text{Bi}_4\text{NbO}_8\text{Cl}$ which reflects the evolution of spin texture by external electric poling. The extremely complex device characteristics and limited knowledge of the ferroic properties of $\text{Bi}_4\text{NbO}_8\text{Cl}$ call for more efforts for understanding the switching dynamics of $\text{Bi}_4\text{NbO}_8\text{Cl}$ -based and general 2D devices with in-plane ferroelectricity. Further, more evidences to support or disapprove the link between the observed photo galvanic effect and ferroelectricity are needed. Our work also sheds lights on designs of spin-orbitronic and opto-spintronic devices for emerging computing.

3. Experimental Section

Materials: BiOCl (98%), Nb_2O_5 (99.9%), Bi_2O_3 (99.9%), CsCl (99.9%), NaCl (99.5%), $\text{La}(\text{NO}_3)_3 \cdot 6\text{H}_2\text{O}$ (99.99%), $\text{Sr}(\text{NO}_3)_2$ (99%), powder were all purchased from Sigma-Aldrich without further treatment. Mn_2O_3 (98%) powder was purchased from Alfa Aesar without further treatment. Graphite crystals were purchased from HQ Graphene Inc., Netherlands. A Dow-Corning Sylgard 184 silicone elastomer kit was used to synthesize polydimethylsiloxane (PDMS) stamps. Quartz tubes and rods were purchased from Technical Glass Products Inc., USA.

One-side polished 300 nm SiO_2/Si wafers, two-side polished LaAlO_3 (001), one-side polished Al_2O_3 (0001) and one-side polished SrTiO_3 (001) substrates were purchased from MTI Inc., USA. 3-mm-thick BG-38 colored glass bandpass filters were purchased from Edmund Optics Inc. USA and used as the IR absorbers in pyroelectric measurements.

Crystal growth — Solid state reaction: Stoichiometric amount of BiOCl , Nb_2O_5 , Bi_2O_3 powder were mixed and grounded by a pair of agate mortar and pestle, then mounted into a quartz tube. Then the tube was pumped to ≈ 100 mTorr and sealed by hydrogen flame. No protection gas was injected into the tube. The inner diameter of the quartz tube is 3 mm. Around 0.1 g mixed powder was used in each growth batch. The sealed tube was loaded into a horizontal tube furnace and heated in open air. The furnace was ramped to 1050 °C within 5 h, dwelled at 1050 °C for 5 h, then cooled down slowly to 875 °C in 22 h for crystallization, after which the furnace was shut down and the tube was naturally cooled down to room temperature. Translucent yellow crystals with lateral size ≈ 0.1 mm were obtained after shattering the tube.

Crystal growth — Flux method: Pearlite (3.47 g) of CsCl/NaCl was mixed with 0.365 g BiOCl , 0.186 g Nb_2O_5 , and 0.98 g Bi_2O_3 powder, then the mixed powder was grounded and loaded into an alumina

crucible capped by an alumina lid. The capped crucible was loaded into a horizontal tube furnace and heated in open air to 800 °C within 2 h, dwelled at 800 °C for 10 h, then cooled down slowly to 450 °C within 15 h. After reaching 450 °C, the furnace was shut down and cooled down naturally to room temperature. When the reaction was finished, the yellow mixture inside the crucible was soaked in deionized water overnight, then rinsed for several times with deionized water to remove residual flux.

Crystal growth — $\text{La}_{0.67}\text{Sr}_{0.33}\text{MnO}_3$ (LSMO): LSMO was grown on SrTiO_3 (001) or Al_2O_3 (0001) by pulsed laser deposition (PLD) from a homemade target. Stoichiometric mixture of $\text{La}(\text{NO}_3)_3 \cdot 6\text{H}_2\text{O}$, $\text{Sr}(\text{NO}_3)_2$, and Mn_2O_3 powder were mixed, grounded, and baked at ≈ 400 °C for 5 h, then grounded again and pressed at room temperature under 25 MPa into a pellet. After sintering the pellet at 1250 °C in open air for 12 h, a consolidated target was obtained. LSMO were grown in 300 mTorr pure O_2 at ≈ 700 °C for 30 min, with laser wavelength 248 nm, pulse energy ≈ 40 mJ, pulse frequency 10 Hz, and spot size ≈ 2 mm². LSMO film thickness was ≈ 20 nm. LSMO patterns were used as chemically-inert electrodes without any magnetization.

Optical Characterizations: Room-temperature photoluminescence was checked with a Picoquant 405 nm pulsed diode laser, a Nikon Eclipse Ti-S inverted optical microscope, a Thorlabs 4 Megapixel Monochrome Scientific CCD Camera, and a Princeton Instruments SP-2358 spectrograph. Cryogenic PL was carried out by gluing the sample in a Linkham THMS600 microscope cryostat. Samples were loaded into cryostat where they were protected in flowing nitrogen at nominally 1 atm. To collect PL signal, 405 nm laser was focused onto individual flake and the signal was collected immediately. Laser intensity was ≈ 0.02 nJ pulse⁻¹. No damage from laser was observed under optical microscope.

SHG Mapping: The excitation light was extracted using an optical parametric oscillator (Maitai SP, Spectra Physics, Santa Clara, USA) pumped by a mode-locked Ti: sapphire oscillator. The excitation laser was 798 nm and linearly polarized by a polarizing beam splitter. The transmission polarized laser light can change its polarization by rotating a 450–800 nm half-wave plate before pumping sample. The laser was focused by a 20 × objective lens onto the sample. A 785 nm short pass filter blocked out the excitation beam. The SHG signal was detected in the backscattering configuration, analyzed by a visible-range polarizer, and finally collected by a cooled CCD spectrometer. For SHG spatial mapping image, a microscope objective lens (Nikon 20 ×, N.A. 0.45) was mounted on a 3D piezostage. The excitation and collection light spot position at the sample plane was scanned by moving the objective lens on the piezostage. A sensitive photomultiplier tube (PMT) was used to analyze the SHG signal in the fast mapping mode.

Fabrication of Microsheet Devices: $\text{Bi}_4\text{NbO}_8\text{Cl}$ single crystals were put onto scotch tape and exfoliated for ≈ 5 to 10 times. Then the newly exfoliated flakes were pressed by a ≈ 2 -mm-thick PDMS stamp. After lifting up the PDMS stamp quickly, some exfoliated crystals could be transferred onto PDMS stamp. Graphite flakes were exfoliated from graphite crystals in the same way. PDMS stamps with exfoliated graphite flakes or $\text{Bi}_4\text{NbO}_8\text{Cl}$ microsheets were loaded onto a three-axis micro manipulator, then aligned to the metal patterns under optical microscope. After gently pressing the flakes (graphite or $\text{Bi}_4\text{NbO}_8\text{Cl}$) onto the desired position, the PDMS stamp was lifted up slowly so that the crystals could leave on the substrate.

Fabrication of Ceramic Disk Device: The as-grown $\text{Bi}_4\text{NbO}_8\text{Cl}$ microcrystals were grounded in an agate mortar and then cold pressed into ceramic disk using a stainless steel die (1/4 inch I.D. Dry Pellet Pressing Die, MTI Corporation) at 2.5 metric tons for 30 min. The thickness of the pellet was ≈ 0.1 mm. The disk was sintered in open air in a muffle furnace set at 200 °C for 5 h to consolidate the disk. Conductive copper tapes or carbon tapes were attached to the top and bottom surfaces of the consolidated ceramic disk as electrodes.

Fabrication of Patterned Electrodes: The cleaned substrates were patterned by mask-less lithography (Intelligent Micro Patterning model SF-100 Lightning Plus, positive photoresist S1813). Ti (3 nm) and 20 nm Au were then deposited in sequence by e-beam evaporation, onto the

patterned surface of 300 nm SiO₂/Si, c-sapphire, or IR absorber. After lift-off, the patterned substrates with channel distance of 10 to 30 μm were obtained. To make patterned LSMO electrodes, LSMO film grown on sapphire substrates were patterned in the same way, etched with acid solutions to remove LSMO in desired locations, and then rinsed with acetone to remove residual photoresist.

Transport Measurements: *I*–*V* measurements were done by an Autolab PGSTAT302N potentiostat. Silver paste was dropped onto the far end of Au electrodes to improve the contact between Au electrodes and the micro probes of potentiostat. Poling voltage was generated from a Tektronix AFG1022 arbitrary function generator and then amplified by a Falco WMA-02 high voltage amplifier.

In photogalvanic effect measurements, a 405 nm quarter wave plate was fixed to a homemade motor that rotates 360° every 29 s. The laser beam was passed through the quarter wave plate and shone onto different devices. No lock-in technique was applied in photogalvanic effect measurements.

The visible laser used in all transport measurements was a Thorlabs LDM405 diode laser, wavelength 405 nm, output power ≈ 4 mW. The beam (spot size ≈ 3.0 mm × 5.0 mm) was directly shone onto the crystal without further focusing. The spot size was much larger than crystal size.

In dynamic pyroelectric measurements, IR laser beam was generated from a DILAS mTf4s22-1064 fiber-coupled diode laser with central wavelength 1064 nm and output power ≈ 5 W, and was focused by two long-focus convex lenses as well as the 20 × objective lens of optical microscope, and eventually, a laser spot with diameter ≈ 105 μm was shone onto the micro device. The laser beam was chopped at 133 Hz to generate periodic heating cycles. The microdevice was connected into a Stanford Research SR830 DSP lock-in amplifier onto which the chopper was connected as reference signal. During pyroelectric coefficient versus poling electric field loop measurement, the devices were poled at a series of voltages: 500, 1000, 1500, 2000, 2500, 2000, 1500, 1000, 500, 0, –500, –1000, –1500, –2000, –2500, –2000, –1500, –1000, –500, and 0 V consecutively. After each poling process, pyroelectric currents were measured using the potentiostat and the cyrostage. The temperature of the devices was increased from 25 to 50 °C with a ramp speed of 50 °C min^{–1}, and pyroelectric coefficient was calculated by integrating the current: $I = A\alpha \frac{dT}{dt} \rightarrow Q = A\alpha(T_2 - T_1)$, where *I* stands for current, *A* is device area, α represents pyroelectric coefficient, *Q* is the charges obtained by integration, and *T*₁ and *T*₂ are starting and ending temperatures.

XRD, AFM, SEM, and EDX: A Panalytical X'pert PRO MPD system with a Cu source that yields $\lambda_{K\alpha 1} = 1.5406$ Å beam was used for XRD studies. The surface morphologies of flakes were examined under tapping mode. The AFM tip (TAP300AL) was purchased from Ted Pella Inc. USA. SEM/EDS were collected with a Zeiss SUPRA 55 system.

FIB and TEM: A Helios G4 UX Focused Ion Beam (FIB) was utilized to prepare cross-section TEM samples. Electron diffraction patterns and high-resolution TEM images were taken at room temperature with an FEI F20 TEM operated at 200 kV. Diffraction patterns were simulated by ReciPro.

DFT Computation: The calculations were performed using density functional theory (DFT) based Vienna Ab initio Simulation Package.^[40] The electron-ion interaction was described using projector augmented wave (PAW) method.^[41] The exchange correlation between electrons was treated with generalized gradient approximation (GGA) in the Perdew–Burke–Ernzerhof (PBE) form.^[42] An energy cutoff of 400 eV was used for the plane wave basis set. In sampling the Brillouin zone integrations, Monkhorst–Pack *k*-point meshes were used with a reciprocal space resolution of $2\pi \times 0.03$ Å^{–1}.^[43] The experimentally determined structure was used without further relaxation.

High-Resolution Atomic Force Microscopy (HRAFM): The surface morphologies were investigated by high-resolution atomic force microscopy (AFM, Cypher ES, Oxford Instruments) in ambient air. To derive the atomic-scale structures of the crystallite surface, a sharp Si₃N₄ probe (TR400PB, Olympus) was used in the contact mode. The lateral force signal was recorded in order to atomically resolve the recorded

image as the friction force is sensitive to the evolution of surface crystal lattice. To avoid surface damage, the applied normal load was controlled in the range of 10–20 nN and the sliding velocity was set at 10–15 Hz. The recorded image was processed by the Asylum Research Igor Pro Software.

Supporting Information

Supporting Information is available from the Wiley Online Library or from the author.

Acknowledgements

The authors thank Sarah An from RPI Micro and Nano Fabrication Clean Room for technical support in optical lithography. Z.C. and Y.H. thank financial supports from NSF under award numbers 1706815 and 1916652. L.Z. thanks the financial support from the NYSTAR Focus Center at Rensselaer Polytechnic Institute under award number C180117, and Y.G., R.J., and J.S. thank the financial support from the Air Force Office of Scientific Research under award number FA9550-18-1-0116. The authors also thank the financial supports from US NSF under award numbers of 1629230 and 2031692. S.M. and H.Z. thank the support from NSF under award number 2005096. L.G. thanks the National Key Research and Development Program of China (No. 2018YFB0704300). This material is also partially based on work supported by the NSF-MIP Platform for the Accelerated Realization, Analysis, and Discovery of Interface Materials (PARADIM) under cooperative agreement no. DMR-2039380. Y.-Y.S. thanks the support from Shanghai International Cooperation Project (20520760900). Z.C. and J.S. thank Prof. Minoru Tomozawa for the use of his lab furnace.

Conflict of Interest

The authors declare no conflict of interest.

Data Availability Statement

The data that support the findings of this study are available from the corresponding author upon reasonable request.

Keywords

electric field, oxyhalide, semiconductors, spin, switching

Received: June 3, 2022

Revised: August 12, 2022

Published online:

- [1] H. Ohno, D. Chiba, F. Matsukura, T. Omiya, E. Abe, T. Dietl, Y. Ohno, K. Ohtani, *Nature* **2000**, 408, 944.
- [2] K. L. Wang, X. Kou, P. Upadhyaya, Y. Fan, Q. Shao, G. Yu, P. K. Amiri, *Proc. of the IEEE* **2016**, 104, 1974.
- [3] G. Lawes, G. Srinivasan, *J. Phys. D: Appl. Phys.* **2011**, 44, 243001.
- [4] a) N. A. Hill, *J. Phys. Chem. B* **2000**, 104, 6694; b) N. A. Spaldin, R. Ramesh, *Nat. Mater.* **2019**, 18, 203.
- [5] C. Song, B. Cui, F. Li, X. Zhou, F. Pan, *Prog. Mater. Sci.* **2017**, 87, 33.
- [6] A. Sasaki, S. Nonaka, Y. Kunihashi, M. Kohda, T. Bauernfeind, T. Dollinger, K. Richter, J. Nitta, *Nat. Nanotechnol.* **2014**, 9, 703.

- [7] M. Kohda, G. Salis, *Semicond. Sci. Technol.* **2017**, *32*, 073002.
- [8] a) S. D. Ganichev, L. E. Golub, *Physica Status Solidi* **2014**, *251*, 1801; b) X. Zhang, Q. Liu, J.-W. Luo, A. J. Freeman, A. Zunger, *Nat. Phys.* **2014**, *10*, 387.
- [9] P. Noël, F. Trier, L. M. Vicente Arche, J. Bréhin, D. C. Vaz, V. Garcia, S. Fusil, A. Barthélémy, L. Vila, M. Bibes, J.-P. Attané, *Nature* **2020**, *580*, 483.
- [10] S. Datta, B. Das, *Appl. Phys. Lett.* **1990**, *56*, 665.
- [11] D. Di Sante, P. Barone, R. Bertacco, S. Picozzi, *Adv. Mater.* **2013**, *25*, 509.
- [12] a) V. Garcia, M. Bibes, L. Bocher, S. Valencia, F. Kronast, A. Crassous, X. Moya, S. Enouz-Vedrenne, A. Gloter, D. Imhoff, *Science* **2010**, *327*, 1106; b) A. Soumyanarayanan, N. Reyren, A. Fert, C. Panagopoulos, *Nature* **2016**, *539*, 509; c) J. R. Sánchez, L. Vila, G. Desfonds, S. Gambarelli, J. Attané, J. De Teresa, C. Magén, A. Fert, *Nat. Commun.* **2013**, *4*, 2944; d) J. Mclver, D. Hsieh, H. Steinberg, P. Jarillo-Herrero, N. Gedik, *Nat. Nanotechnol.* **2012**, *7*, 96; e) A. Caviglia, M. Gabay, S. Gariglio, N. Reyren, C. Cancellieri, J.-M. Triscone, *Phys. Rev. Lett.* **2010**, *104*, 126803; f) J. Nitta, T. Akazaki, H. Takayanagi, T. Enoki, *Phys. Rev. Lett.* **1997**, *78*, 1335; g) A. Manchon, H. C. Koo, J. Nitta, S. Frolov, R. Duine, *Nat. Mater.* **2015**, *14*, 871; h) Y. Jia, M. Zhao, G. Gou, X. C. Zeng, J. Li, *Nanoscale Horiz.* **2019**, *4*, 1113.
- [13] a) M. Liebmann, C. Rinaldi, D. Di Sante, J. Kellner, C. Pauly, R. N. Wang, J. E. Boschker, A. Giussani, S. Bertoli, M. Cantoni, *Adv. Mater.* **2016**, *28*, 560; b) C. Rinaldi, S. Varotto, M. Asa, J. Sławińska, J. Fujii, G. Vinai, S. Cecchi, D. Di Sante, R. Calarco, I. Vobornik, *Nano Lett.* **2018**, *18*, 2751; c) S. Varotto, L. Nessi, S. Cecchi, J. Sławińska, P. Noël, S. Petró, F. Fagiani, A. Novati, M. Cantoni, D. Petti, E. Albisetti, M. Costa, R. Calarco, M. Buongiorno Nardelli, M. Bibes, S. Picozzi, J.-P. Attané, L. Vila, R. Bertacco, C. Rinaldi, *Nat. Electron.* **2021**, *4*, 740.
- [14] N. A. Benedek, J. M. Rondinelli, H. Djani, P. Ghosez, P. Lightfoot, *Dalton Trans.* **2015**, *44*, 10543.
- [15] a) J. Zylberberg, A. A. Belik, E. Takayama-Muromachi, Z.-G. Ye, *Chem. Mater.* **2007**, *19*, 6385; b) L. G. D. da Silveira, P. Barone, S. Picozzi, *Phys. Rev. B* **2016**, *93*, 245159.
- [16] C. Autieri, P. Barone, J. Sławińska, S. Picozzi, *Phys. Rev. Mater.* **2019**, *3*, 084416.
- [17] L. L. Tao, T. R. Paudel, A. A. Kovalev, E. Y. Tsymlal, *Phys. Rev. B* **2017**, *95*, 245141.
- [18] a) K. Ogawa, A. Nakada, H. Suzuki, O. Tomita, M. Higashi, A. Saeki, H. Kageyama, R. Abe, *ACS Appl. Mater. Interfaces* **2019**, *11*, 5642; b) H. Kunioku, A. Nakada, M. Higashi, O. Tomita, H. Kageyama, R. Abe, *Sustainable Energy Fuels* **2018**, *2*, 1474; c) H. Fujito, H. Kunioku, D. Kato, H. Suzuki, M. Higashi, H. Kageyama, R. Abe, *J. Am. Chem. Soc.* **2016**, *138*, 2082; d) H. Suzuki, H. Kunioku, M. Higashi, O. Tomita, D. Kato, H. Kageyama, R. Abe, *Chem. Mater.* **2018**, *30*, 5862; e) C. Zhong, D. Kato, F. Takeiri, K. Fujii, M. Yashima, E. Nishiwaki, Y. Fujii, A. Koreeda, C. Tassel, R. Abe, H. Kageyama, *Inorganics* **2018**, *6*, 41.
- [19] A. M. Kusainova, S. Y. Stefanovich, V. A. Dolgikh, A. V. Mosunov, C. H. Hervoches, P. Lightfoot, *J. Mater. Chem.* **2001**, *11*, 1141.
- [20] H. Ai, X. Ma, X. Shao, W. Li, M. Zhao, *Phys. Rev. Mater.* **2019**, *3*, 054407.
- [21] a) X. Meng, Z. Li, H. Zeng, J. Chen, Z. Zhang, *Appl. Catal., B* **2017**, *210*, 160; b) H.-P. Wang, S. Li, X. Liu, Z. Shi, X. Fang, J.-H. He, *Adv. Mater.* **2021**, *33*, 2003309.
- [22] M. Liao, Y. Zhu, J. Zhang, R. Zhong, J. Schneeloch, G. Gu, K. Jiang, D. Zhang, X. Ma, Q.-K. Xue, *Nano Lett.* **2018**, *18*, 5660.
- [23] S. S. Cheema, N. Shanker, S.-L. Hsu, Y. Rho, C.-H. Hsu, V. A. Stoica, Z. Zhang, J. W. Freeland, P. Shafer, C. P. Grigoropoulos, J. Ciston, S. Salahuddin, *Science* **2022**, *376*, 648.
- [24] A. S. Sigov, M. I. Maletto, E. P. Pevtsov, V. V. Chernokozhin, *Ferroelectrics* **1999**, *226*, 183.
- [25] Y. Uesu, S. Kurimura, Y. Yamamoto, *Appl. Phys. Lett.* **1995**, *66*, 2165.
- [26] a) S. Li, Y. Zhang, W. Yang, H. Liu, X. Fang, *Adv. Mater.* **2020**, *32*, 1905443; b) X. Liu, S. Li, Z. Li, Y. Zhang, W. Yang, Z. Li, H. Liu, D. V. Shtansky, X. Fang, *Adv. Funct. Mater.* **2021**, *31*, 2101480.
- [27] a) Y. Yamada, Y. Kanemitsu, J. Lumin. **2013**, *133*, 30; b) Y. Yamada, H. Yasuda, T. Tayagaki, Y. Kanemitsu, *Phys. Rev. Lett.* **2009**, *102*, 247401; c) Y. Kanemitsu, Y. Yamada, *Chem. – Asian J.* **2020**, *15*, 709.
- [28] a) G.-L. Yuan, J. Wang, *Appl. Phys. Lett.* **2009**, *95*, 252904; b) C. Ge, C. Wang, K.-j. Jin, H.-b. Lu, G.-z. Yang, *Nano-Micro Lett.* **2013**, *5*, 81; c) C. Wang, K.-j. Jin, Z.-t. Xu, L. Wang, C. Ge, H.-b. Lu, H.-z. Guo, M. He, G.-z. Yang, *Appl. Phys. Lett.* **2011**, *98*, 192901; d) T. Choi, S. Lee, Y. J. Choi, V. Kiryukhin, S.-W. Cheong, *Science* **2009**, *324*, 63; e) Z. Chen, Y. Hu, L. Zhang, J. Jiang, R. Hawks, J. Shi, *Appl. Phys. Lett.* **2021**, *119*, 033103; f) N. Higashitarumizu, H. Kawamoto, C.-J. Lee, B.-H. Lin, F.-H. Chu, I. Yonemori, T. Nishimura, K. Wakabayashi, W.-H. Chang, K. Nagashio, *Nat. Commun.* **2020**, *11*, 2428.
- [29] Z. Xiao, Y. Yuan, Y. Shao, Q. Wang, Q. Dong, C. Bi, P. Sharma, A. Gruverman, J. Huang, *Nat. Mater.* **2015**, *14*, 193.
- [30] M. H. Park, Y. H. Lee, T. Mikolajick, U. Schroeder, C. S. Hwang, *MRS Commun.* **2018**, *8*, 795.
- [31] Y. Zhou, H. K. Chan, C. H. Lam, F. G. Shin, *J. Appl. Phys.* **2005**, *98*, 024111.
- [32] a) S. D. Ganichev, S. Ganichev, W. Prettl, *Intense Terahertz Excitation of Semiconductors*, Oxford University Press on Demand, Oxford **2006**; b) M. I. Dyakonov, *Spin Physics in Semiconductors*, Springer, Cham, Switzerland **2017**.
- [33] a) L. Liu, E. J. Lenferink, G. Wei, T. K. Stanev, N. Speiser, N. P. Stern, *ACS Appl. Mater. Interfaces* **2019**, *11*, 3334; b) H. Guan, N. Tang, H. Huang, X. Zhang, M. Su, X. Liu, L. Liao, W. Ge, B. Shen, *ACS Nano* **2019**, *13*, 9325.
- [34] a) J. Quereda, T. S. Ghiasi, J.-S. You, J. van den Brink, B. J. van Wees, C. H. van der Wal, *Nat. Commun.* **2018**, *9*, 3346; b) Z. Ji, G. Liu, Z. Addison, W. Liu, P. Yu, H. Gao, Z. Liu, A. M. Rappe, C. L. Kane, E. J. Mele, R. Agarwal, *Nat. Mater.* **2019**, *18*, 955.
- [35] a) L. Luo, L. Men, Z. Liu, Y. Mudryk, X. Zhao, Y. Yao, J. M. Park, R. Shinar, J. Shinar, K.-M. Ho, I. E. Perakis, J. Vela, J. Wang, *Nat. Commun.* **2017**, *8*, 15565; b) D. Niesner, M. Hauck, S. Shrestha, I. Levchuk, G. J. Matt, A. Osvet, M. Batentschuk, C. Brabec, H. B. Weber, T. Fauster, *Proc. Natl. Acad. Sci. USA* **2018**, *115*, 9509; c) X. Liu, A. Chanana, U. Huynh, F. Xue, P. Haney, S. Blair, X. Jiang, Z. V. Vardeny, *Nat. Commun.* **2020**, *11*, 323.
- [36] H. Diehl, V. A. Shalygin, V. V. Bel'kov, C. Hoffmann, S. N. Danilov, T. Herrle, S. A. Tarasenko, D. Schuh, C. Gerl, W. Wegscheider, W. Prettl, S. D. Ganichev, *New J. Phys.* **2007**, *9*, 349.
- [37] a) Y. Kamata, S. Kurimura, Y. Uesu, B. A. Strukov, *Jpn. J. Appl. Phys.* **1994**, *33*, 5453; b) A. A. Grinberg, S. Luryi, *Phys. Rev. B* **1988**, *38*, 87.
- [38] S. D. Ganichev, E. L. Ivchenko, V. V. Bel'kov, S. A. Tarasenko, M. Sollinger, D. Weiss, W. Wegscheider, W. Prettl, *Nature* **2002**, *417*, 153.
- [39] J. Nitta, T. Akazaki, H. Takayanagi, T. Enoki, *Phys. Rev. Lett.* **1997**, *78*, 1335.
- [40] G. Kresse, J. Furthmüller, *Phys. Rev. B* **1996**, *54*, 11169.
- [41] G. Kresse, D. Joubert, *Phys. Rev. B* **1999**, *59*, 1758.
- [42] J. P. Perdew, K. Burke, M. Ernzerhof, *Phys. Rev. Lett.* **1996**, *77*, 3865.
- [43] H. J. Monkhorst, J. D. Pack, *Phys. Rev. B* **1976**, *13*, 5188.